Nanoscale domain engineering in SrRuO$_3$ thin films

Céline Lichtensteiger ✉ (iD) ; Chia-Ping Su (iD) ; Iaroslav Gaponenko (iD) ; Marios Hadjimichael (iD) ;
Ludovica Tovaglieri (iD) ; Patrycja Paruch (iD) ; Alexandre Gloter (iD) ; Jean-Marc Triscone (iD)

Check for updates

View Online   Export Citation   CrossMark

Articles You May Be Interested In

Mapping the complex evolution of ferroelastic/ferroelectric domain patterns in epitaxially strained PbTiO$_3$ heterostructures

APL Mater (June 2023)

Atomic scale investigation of a PbTiO$_3$/SrRuO$_3$/DyScO$_3$ heterostructure

Appl. Phys. Lett. (June 2013)

Self-assembly and properties of domain walls in BiFeO$_3$ layers grown via molecular-beam epitaxy
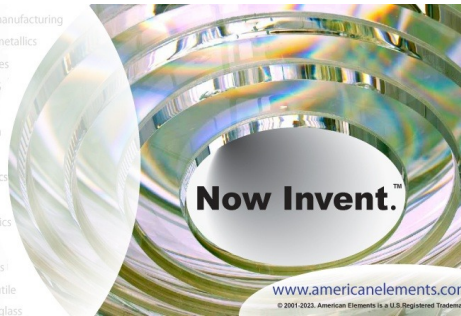
APL Mater (July 2019)

Nanoscale domain engineering in SrRuO₃ thin films

View Online   Export Citation   CrossMark

Céline Lichtensteiger,[1,a] (ID) Chia-Ping Su,[2] (ID) Iaroslav Gaponenko,[1] (ID) Marios Hadjimichael,[1] (ID) Ludovica Tovaglieri,[1] (ID) Patrycja Paruch,[1] (ID) Alexandre Gloter,[2] (ID) and Jean-Marc Triscone[1] (ID)

AFFILIATIONS

[1] Department of Quantum Matter Physics, University of Geneva, 24 Quai Ernest-Ansermet, CH-1211 Geneva 4, Switzerland

[2] Université Paris-Saclay, CNRS, Laboratoire de Physique des Solides, Orsay 91405, France

[a] Author to whom correspondence should be addressed: Celine.Lichtensteiger@unige.ch

ABSTRACT

We investigate nanoscale domain engineering via epitaxial coupling in a set of SrRuO₃/PbTiO₃/SrRuO₃ heterostructures epitaxially grown on $(110)_o$-oriented DyScO₃ substrates. The SrRuO₃ layer thickness is kept at 55 unit cells, whereas the PbTiO₃ layer is grown to thicknesses of 23, 45, and 90 unit cells. Through a combination of atomic force microscopy, x-ray diffraction, and high resolution scanning transmission electron microscopy studies, we find that above a certain critical thickness of the ferroelectric layer, the large structural distortions associated with the ferroelastic domains propagate through the top SrRuO₃ layer, locally modifying the orientation of the orthorhombic SrRuO₃ and creating a modulated structure that extends beyond the ferroelectric layer boundaries.

I. INTRODUCTION

Ferroelectric polarization can be used to affect the properties of other materials. This is well known in ferroelectric field-effect transistors, for example, where the polarization surface charge of the ferroelectric film is used to reversibly dope the adjacent layer, as demonstrated in epitaxial oxide thin film heterostructures.[1]

In this work, a PbTiO₃ layer is sandwiched between two SrRuO₃ layers. In bulk, SrRuO₃ is a ferromagnetic metallic transition-metal oxide and is often used as an electrode in the ferroelectric oxides community.[2] It is also an itinerant ferromagnet with a Curie temperature $T_C = 160$ K.[3] In thin films of this material, the formation of complex spin textures can be induced by the ferroelectric polarization in an adjacent ferroelectric layer. These include the ferroelectric proximity effect near the BaTiO₃/SrRuO₃ interface giving rise to an emergent Dzyaloshinskii–Moriya interaction, thereby creating robust magnetic skyrmions.[4] Most recently, in SrRuO₃/PbTiO₃ heterostructures, a ferroelectrically induced magnetic spin crystal was observed.[5]

SrRuO₃ is not only affected by the polarization in adjacent layers but also by the epitaxial strain imposed by the substrate.[6,7] When grown on SrTiO₃, epitaxial SrRuO₃ layers are organized into structural domains, according to six possible orientations of the orthorhombic unit cell with respect to the cubic substrate. The orientation of the orthorhombic unit cell and resulting domain strucutre are affected by the steps and terraces at the surface of the SrTiO₃ substrate.[8] The growth of SrRuO₃ onto the vicinal planes of miscut SrTiO₃ substrates leads to the privileged development of a majority single domain orientation in which small domains with different orientations are embedded.[9] In addition, control of the SrRuO₃ can be achieved not only through the choice of substrate[10] but also by modifying the growth temperature.[11] Further structural domain engineering has been conducted through control of substrate miscut direction, demonstrating a one-to-one correspondence between structural domains and magnetic domains.[12]

A structural coupling can also be achieved by strain propagation between the different layers themselves. As was shown in PbTiO₃/SrTiO₃/PbTiO₃ heterostructures on GdScO₃, where the structural coupling between the PbTiO₃ and SrTiO₃ layers resulted in periodic polar waves in the SrTiO₃,[13] in SrRuO₃/PbTiO₃ superlattices, the large local deformations of the ferroelectric lattice are accommodated by periodic lattice modulations of the metallic SrRuO₃ layers with very large curvatures.[14]

At the core of the heterostructure studied here is PbTiO₃, a tetragonal ferroelectric with a polarization developing along the c-axis mostly due to ionic displacements. In PbTiO₃ thin films,

the orientation of the polarization and arrangement into domain structures have been theoretically studied,[15–20] and are described by phase diagrams with regions of different domain configurations as a function of epitaxial strain and temperature (see review by Schlom et al.[21]). The domain pattern is also affected by the film thickness[22] and electrostatic boundary conditions.[23,24] Complex polarization configurations in PbTiO₃ have recently been reported in PbTiO₃/SrTiO₃ superlattices,[14,25–30] with simultaneous control of these configurations using electric fields and light, giving rise to novel phenomena such as negative capacitance.[31] When grown on DyScO₃, PbTiO₃ takes the a/c phase, where the polarization forms ordered ferroelastic domains (a/c twins), resulting in distortions of the film surface visible by atomic force microscopy (AFM).[32–35]

Whether through ferroelectric polarization or strain effects, controlling the structure and morphology of the SrRuO₃ thin films is of importance as it will affect the film electronic resistivity via structural and electronic coupling. Here, we study the structural coupling between oxide thin film layers on a set of SrRuO₃/PbTiO₃/SrRuO₃ heterostructures epitaxially grown on (110)ₒ-oriented DyScO₃ substrates. We establish the direct role that the ferroelastic domain structure in PbTiO₃ plays in the determination of the orthorhombic domain structure in SrRuO₃.

II. RESULTS

A series of samples was grown by off-axis radio-frequency (RF) magnetron sputtering on (110)ₒ-oriented DyScO₃ substrates, with

the bottom and top SrRuO₃ electrodes of 55 unit cells (u.c.) and a PbTiO₃ film thickness of 23, 45, and 90 u.c. (see Sec. IV A for details of sample growth).

The substrate, DyScO₃, is orthorhombic with room temperature lattice parameters (in the *Pbnm* space group) $a_o = 5.443(2)$ Å, $b_o = 5.717(2)$ Å, and $c_o = 7.901(2)$ Å.[36] It is often useful to also refer to the pseudocubic unit cell, where the lattice parameters can be calculated as $a_{pc} = c_{pc} = \frac{\sqrt{a_o^2 + b_o^2}}{2} = 3.947$ Å, $b_{pc} = c_o/2 = 3.951$ Å, $\alpha_{pc} = \gamma_{pc} = 90°$, and $\beta_{pc} = 2 \cdot \arctan(a_o/b_o) = 87.187°$ at room temperature. Here, "pc" subscript refers to the pseudocubic unit cell, while "o" is used to refer to the orthorhombic unit cell. For (110)ₒ-oriented DyScO₃, the out-of-plane $[001]_{pc}$ direction is equivalent to $[110]_o$, while the in-plane directions $[100]_{pc}$ and $[010]_{pc}$ are equivalent to $[\bar{1}10]_o$ and $[001]_o$, respectively (see the supplementary material, Fig. S1).

The bottom and top electrodes, SrRuO₃, are orthorhombic with bulk room temperature lattice parameters (in the *Pbnm* space group) $a_o = 5.57$ Å, $b_o = 5.53$ Å, and $c_o = 7.85$ Å,[37] corresponding to the pseudocubic unit cell parameters $a_{pc} = c_{pc} = 3.924$ Å, $b_{pc} = 3.925$ Å, $\alpha_{pc} = \gamma_{pc} = 90°$, and $\beta_{pc} = 90.413°$. According to the Glazer notation, octahedral tilting in orthorhombic SrRuO₃ is described by $a^-a^-c^+$, implying that RuO₆ octahedra are rotated in opposite directions by equivalent magnitude along $[100]_{pc}$ and $[010]_{pc}$ (out-of-phase) and in the same direction about $[001]_{pc}$ (in-phase).[38,39] On (110)ₒ-oriented DyScO₃ substrate, SrRuO₃ can grow with different possible orientations,[8,12] as described in Fig. 1, and supplementary material, Figs. S1 and S2.
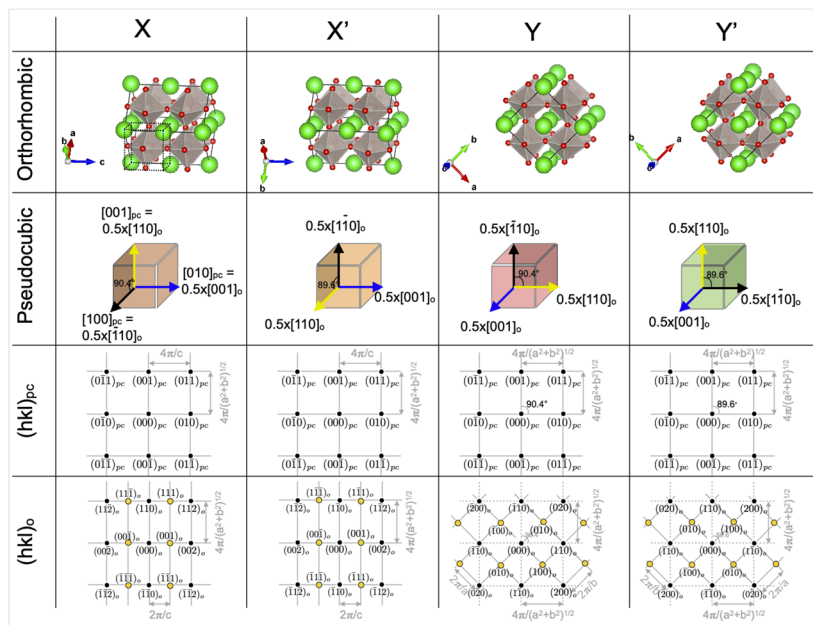
FIG. 1. Detailed representation of four of the possible orthorhombic orientations of the SrRuO₃ on the (110)ₒ-oriented DyScO₃ substrate (in the *Pbnm* space group). Each column corresponds to a different orientation: X, X', Y, and Y'. First row: perspective view, with arrows $\vec{a} \parallel [100]_o$, $\vec{b} \parallel [010]_o$ and $\vec{c} \parallel [001]_o$ corresponding to the axis of the orthorhombic unit cell. Second row: corresponding pseudocubic representation. Third row: reciprocal space representation and (hkl) indices corresponding to the pseudocubic structure. Fourth row: reciprocal space representation and (hkl) indices corresponding to the orthorhombic structure, highlighting the position of the "half-order" peaks. The six possible orthorhombic orientations can be found in supplementary material, Figs S1 and S2.

Last, the PbTiO$_3$ is ferroelectric below a bulk critical temperature of 765 K with a tetragonal structure and lattice parameters $a = b = 3.904$ Å and $c = 4.152$ Å at room temperature. The in-plane strain imposed by DyScO$_3$ on PbTiO$_3$ films can thus be calculated as $\frac{a_{pc}-a_0}{a_{pc}} = -0.25\%$ along a_{pc} and $\frac{b_{pc}-a_0}{b_{pc}} = -0.16\%$ along b_{pc}, where a_0 is the extrapolated lattice parameter of PbTiO$_3$ in the room-temperature cubic paraelectric phase, $a_0 = 3.957$ Å for PbTiO$_3$. To accommodate this strain,[40] PbTiO$_3$ thin films on DyScO$_3$ at room temperature are expected to be in the a/c-phase, with regions where the c-axis points out-of-plane (c-domains) as well as regions where it points in-plane (a-domains), giving rise to a ferroelastic a/c-domain configuration with 90° domain walls. The latter are parallel to the $\{101\}_{pc}$ crystallographic planes and, thus, are inclined at about 45° with respect to the film/substrate interface, as predicted in Ref. 17 and demonstrated experimentally (see, for example, Refs. 33, 34, and 41). In addition to these ferroelastic domains, the electrostatic boundary conditions and depolarization field arising from an incomplete screening of the surface bound charges can lead the c-domains to alternate between "up" (c^+) and "down" (c^-) orientations. Although the surface bound charges of our PbTiO$_3$ films are screened by the top and bottom SrRuO$_3$ electrodes, this screening is incomplete[42–46] and the depolarization field still plays a role. Such a combination of mechanical and electrostatic constraints can then result in flux-closure structures, as observed in strained PbTiO$_3$ thin films.[35,45,47,48]

A. Topographic modulation observed at the heterostructure surface using atomic force microscopy

Figure 2(a) shows atomic force microscopy (AFM) images for the three SrRuO$_3$/PbTiO$_3$/SrRuO$_3$ heterostructures grown on DyScO$_3$. The AFM topography images reveal that as the PbTiO$_3$ layer thickness increases, trenches develop at the surface of the SrRuO$_3$ top layer in an organized pattern. For the samples with 23 and 45 u.c. thick PbTiO$_3$ layers, this pattern is hardly visible, and the top SrRuO$_3$ is smooth. The pattern gets more pronounced and anisotropic with increasing PbTiO$_3$ layer thickness, with long and deep trenches parallel to the DyScO$_3$ $[001]_o$ axis, and smaller trenches parallel to the DyScO$_3[\bar{1}10]_o$ axis, while the surface roughness stays reasonably low [root mean square (rms) roughness values ranging from 157 to 393 pm over surfaces of $10 \times 10\ \mu m^2$].

The pattern that we observe at the surface of the SrRuO$_3$ top layer is comparable to what has been seen in PbTiO$_3$ layers grown on DyScO$_3$ substrates in Ref. 34, attributed to the presence of periodic ferroelastic a/c domains. To extract the period of the distortions visible on the surface of the samples, we calculate the fast Fourier transform (FFT) of the autocorrelation image, as shown in Fig. 2(d) for the sample with the 90 u.c. thick PbTiO$_3$ layer. Along DyScO$_3$ $[001]_o$ (red), two periods are visible, $P_1 = 77 \pm 1$ nm and $P_2 = 280 \pm 3$ nm, while along DyScO$_3[\bar{1}10]_o$ (blue), a unique period $P_3 = 335 \pm 4$ nm is visible. These periods have been illustrated on the topography image of the corresponding sample as yellow (with dimensions $P_1 \times P_3$) and green (with dimensions $P_2 \times P_3$) rectangles. All these values are reported in Table S1 (supplementary material).
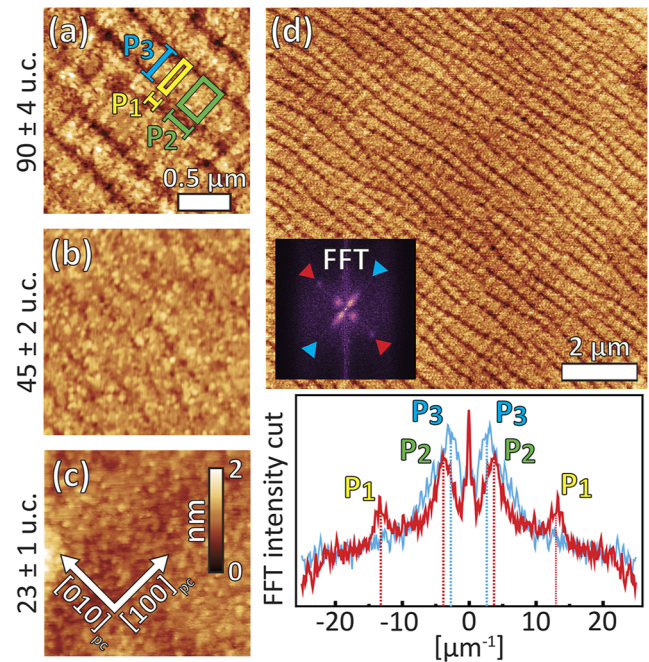

FIG. 2. AFM topography images obtained on the different samples. The color scale varies between 0 and 2 nm. The sample orientation was fixed with respect to the substrate pseudocubic axis $[100]_{pc}//$DyScO$_3[\bar{1}10]_o$ and $[010]_{pc}//$DyScO$_3[001]_o$. (a)–(c) $2 \times 2\ \mu m^2$ scans for the three samples: (a) 90 ± 4 u.c., (b) 45 ± 2 u.c. and (c) 23 ± 1 u.c. thick PbTiO$_3$ between top and bottom SrRuO$_3$ electrodes (55 ± 2 u.c. thick) on DyScO$_3$ substrates, showing that as the PbTiO$_3$ layer thickness increases, trenches develop at the surface of the SrRuO$_3$ top layer. (d) A larger 10 $\times$ 10 μm^2 scan for the 90 u.c. thick PbTiO$_3$ sample displays the anisotropic pattern, with long and deep trenches parallel to the $[010]_{pc}$ axis, and smaller trenches parallel to the $[100]_{pc}$ axis. In the image obtained from the fast Fourier transform of the topography measurement (inset), periodic peaks along $[100]_{pc}$ and $[010]_{pc}$ are visible (see cuts), allowing us to determine the periods. Along $[010]_{pc}$ (red), two periods are visible, $P_1 = 77 \pm 1$ nm and $P_2 = 280 \pm 3$ nm, while along $[100]_{pc}$ (blue), a unique period $P_3 = 335 \pm 4$ nm is visible. These sizes have been drawn on the topography image (a) of the corresponding sample as yellow and green rectangles.

B. Domain structures observed by scanning transmission electron microscopy

To better understand the origin of this pattern visible at the surface of the SrRuO$_3$ top layer, we turned to cross-sectional scanning transmission electron microscopy (STEM) images. The three samples were cut and prepared for STEM measurements to obtain slices in the plane defined by the $[001]_o$ (horizontal direction) and $[110]_o$ (vertical direction) axes of DyScO$_3$. STEM images were obtained using bright field (BF), annular bright field (ABF), medium angle annular dark field (MAADF) and high-angle annular dark field (HAADF) detectors along the DyScO$_3$ $[\bar{1}10]_o$ zone-axis (see Sec. IV C for more technical details).

The domain walls in the PbTiO$_3$ layers can be directly seen in the STEM images, as shown in Fig. 3 [(a)–(c) - HAADF images] and in Fig. 6 [(a)–(c) - BF images], while the SrRuO$_3$ layers appear rather homogeneous. The PbTiO$_3$ layers in the three samples studied have different domain configurations, where the expected a/c
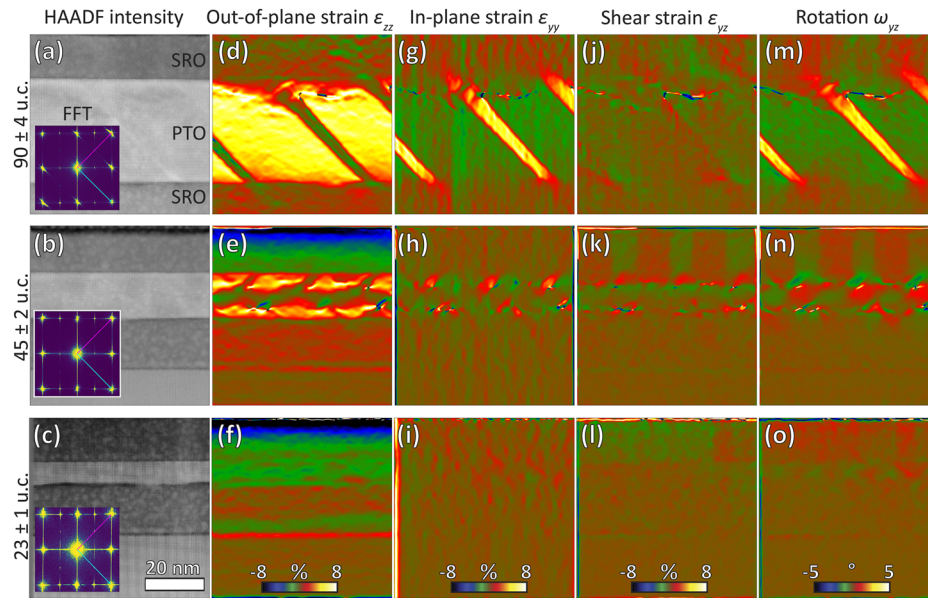
FIG. 3. HAADF images and strain maps for the three samples: (top row) 90±4 u.c., (center row) 45±2 u.c., and (bottom row) 23±1 u.c. thick PbTiO$_3$ between top and bottom SrRuO$_3$ electrodes (55±2 u.c. thick) on DyScO$_3$ substrates. (a)–(c) HAADF images, with the inset showing the FFT and the two vectors used for the GPA analysis indicated by the blue and purple arrows. (d)–(f) Out-of-plane strain ε_{zz}. (g)–(i) In-plane strain ε_{yy}. (j)–(l) Shear strain ε_{yz}. (m)–(o) Rotation ω_{yz}. The strain and rotation values are calculated with respect to a reference lattice here chosen as the substrate. The same intensity scales from −8% to 8% (strain) and from −5° to 5° (rotation) are used for the three samples to allow for comparison. Different contrasts are observed in the PbTiO$_3$ layers, corresponding to the different ferroelastic domain configurations, from a/c for the thickest to flux-closure for the thinner one. The images interestingly reveal an additional contrast appearing only in the top SrRuO$_3$ layers, for the samples with the 45 u.c. and the 90 u.c. thick PbTiO$_3$ layers, and propagating all the way to the top surface.

pattern for the thicker PbTiO$_3$ layer transforms into a flux-closure pattern for the thinner PbTiO$_3$ layers [see Ref. 35 for a complete x-ray diffraction (XRD) based investigation of ferroelectric domain configuration in an extended series of samples].

1. Geometric phase analysis

To study the local strain induced by these different domain configurations, we turn to Geometric Phase Analysis (GPA).[49] This is done by taking the FFT of the HAADF-STEM images in Fig. 3, selecting two peaks [here $(01\bar{1})_{pc}$ and $(011)_{pc}$] corresponding to two reciprocal lattice vectors defining the lattice, and getting the inverse Fourier transform containing information about local displacements of the atomic planes along these two vectors. The local strain components are calculated from the derivative of the obtained displacement field: in-plane strain ε_{yy} (along DyScO$_3$[001]$_o$), out-of-plane strain ε_{zz} (along DyScO$_3$[110]$_o$), shear strain ε_{yz} and rotation ω_{yz}.

Looking first at the results within the PbTiO$_3$ layers, we see from the HAADF images and from the GPA maps that the domain patterns vary with PbTiO$_3$ thickness. For the 90 u.c. thick PbTiO$_3$ in Fig. 3 (top row), we see large regions with a high out-of-plane strain but low in-plane strain, shear and rotation, corresponding to c-domains, i.e., regions where the polarization is out-of-plane. These regions are separated by narrower features, with high in-plane strain, and rotation, but low out-of-plane strain and shear, corresponding to a-domains, i.e., regions where the polarization is in-plane. These results confirm a typical well developed a/c-phase. For the 45 u.c. thick PbTiO$_3$ layer in Fig. 3 (center row), the strain

map is more complex, with alternating regions with large out-of-plane strain or large in-plane strain close to each interface, and reduced strain at the center of the PbTiO$_3$ layer, clearly different from an a/c-phase (see the supplementary material, Fig. S4). This pattern is more comparable to the flux closure configuration observed for PbTiO$_3$ with similar thickness grown without electrodes.[47] Finally, for the 23 u.c. thick PbTiO$_3$ layer in Fig. 3 (bottom row), the PbTiO$_3$ strain maps are more homogeneous compared to the results obtained for the two other samples. This indicates that for this sample, the distortions related to the ferroelectric/ferroelastic domain configuration in the PbTiO$_3$ layer are small with respect to the homogeneous strain induced by the substrate. The most pronounced contrast is visible in the rotation map and corresponds to a pattern with a period of ~16 nm, in agreement with the value found by XRD (see the supplementary material, Fig. S3 and Table S1 for comparison).

Concentrating now on the SrRuO$_3$ layers, we see that the bottom ones are predominantly homogeneous in all three samples. However, this is not the case for the top SrRuO$_3$ layers, where different contrasts appear for the three different PbTiO$_3$ thicknesses. While the SrRuO$_3$ layer on top of the 23 u.c. PbTiO$_3$ looks rather homogeneous, regions with different shear strain and rotation values alternate in the SrRuO$_3$ layers grown on top of the 45 and 90 u.c. PbTiO$_3$ with boundaries propagating along the [001]$_{pc}$ growth direction.

For the sample with 90 u.c. PbTiO$_3$, at the interface with each a-domain and above the obtuse angle formed by the a/c domain

wall, the rotation is positive (red), while it is negative (green) above the acute angle [Fig. 3(m)]. The rotation then propagates directly to the top surface along the growth direction. A similar modulation of the rotation is also observed in the SrRuO$_3$ bottom electrode, with positive rotation below the obtuse angle of the a/c domain wall, and negative rotation below the acute angle. However, for the bottom electrode, this modulation is limited to the vicinity of the interface and does not propagate through the whole SrRuO$_3$ bottom electrode thickness, most likely due to substrate clamping.

For the sample with 45 u.c. PbTiO$_3$, regions with a positive rotation (red) alternate with regions with a negative rotation (green) [Fig. 3(n)], with a reduced rotation amplitude compared to the sample with 90 u.c. thick PbTiO$_3$, but with sharper boundaries. The period of this pattern follows the period of the ferroelectric domains underneath.

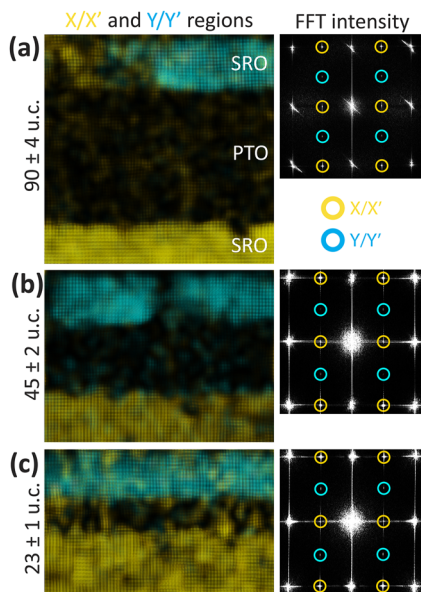### 2. Discriminating between X/X′ and Y/Y′ using fast Fourier transforms

To better understand the origin of this contrast, one can use the FFT and deduce the orientation of the SrRuO$_3$ layers from the obtained Bragg peak positions. In the FFT images in Fig. 4, the bright peaks of the pseudocubic lattice are clearly visible, corresponding to $\{0\ k\ l\}_{pc}$ planes with k and l integer indices. In addition to these peaks, weaker peaks also appear at positions corresponding to planes

FIG. 4. FFT analysis of the SrRuO$_3$ electrodes orientation in the three samples with (a) 90 u.c., (b) 45 u.c., and (c) 23 u.c. thick PbTiO$_3$ layers shows the presence of bright peaks corresponding to the pseudocubic lattice at $\{0\ k\ l\}_{pc}$ with k and l integer indices, and weaker peaks at half-integer Miller indices $\{0\ 1/2\ 1\}_{pc}$, corresponding to X/X' (highlighted in yellow), and $\{0\ 1/2\ 1/2\}_{pc}$, corresponding to Y/Y' orientation (highlighted in blue). The color maps are obtained by FFT filtering the orthorhombic superstructures, demonstrating the X/X' orientation for the bottom SrRuO$_3$ for the three samples, and the Y/Y'-orientation for the top SrRuO$_3$ for the two samples with the thinner PbTiO$_3$ layers (b) and (c) and a mixed X/X'-Y/Y' for the sample with the thickest PbTiO$_3$ layer (a).

with half-integer Miller indices $\{0\ 1/2\ 1/2\}_{pc}$ highlighted in blue and $\{0\ 1/2\ 1\}_{pc}$ highlighted in yellow. These peaks come from the orthorhombic unit cell, which is composed of four pseudocubic unit cells, as described in Fig. 1. The position of the additional peaks is a clear indication of the orientation of the orthorhombic unit cell. The peaks corresponding to the $\{0\ 1/2\ 1\}_{pc}$ planes in the FFT appear when the orthorhombic long axis $[001]_o$ is oriented in-plane, parallel to the $[010]_{pc}$ axis, and correspond to the X or X' orientation (note that it is not possible to discriminate between X or X' in this measurement geometry). The peaks corresponding to the $\{0\ 1/2\ 1/2\}_{pc}$ planes, on the other hand, are the signature of the orthorhombic long axis $[001]_o$ being oriented in-plane, parallel to the $[100]_{pc}$ axis, corresponding to Y or Y' orientation.
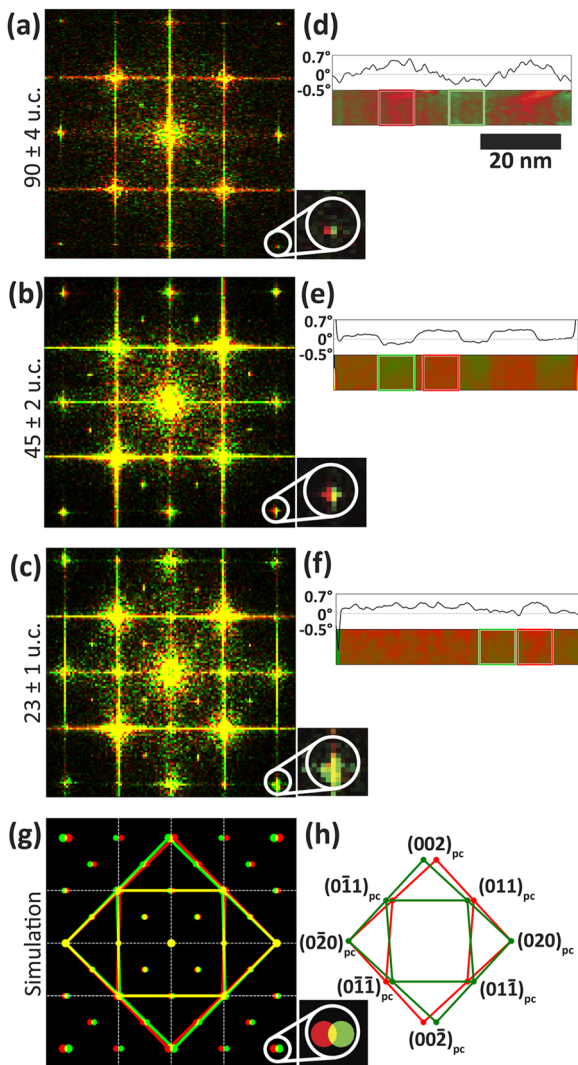
By selecting the different half order peaks and reconstructing the images in Fig. 4, we find that the $\{0\ 1/2\ 1\}_{pc}$ peaks corresponding to X/X' orientation originate from the substrate and the bottom SrRuO$_3$ electrode for all three samples, while the $\{0\ 1/2\ 1/2\}_{pc}$ peaks corresponding to Y/Y' originate from the top SrRuO$_3$ electrode. We also note that for the sample with the thickest PbTiO$_3$ layer, the top SrRuO$_3$ shows a mixed X/X' and Y/Y' character. Although already highlighting differences in the top SrRuO$_3$ layers for the different samples, this is not enough yet to explain the contrast observed in the strain and rotation maps in the GPA analysis in the SrRuO$_3$ top layers for the samples with 45 and 90 u.c. thick PbTiO$_3$ layers. This will be further investigated below, where we show that it is possible to discriminate between Y and Y'.[50]

3. Discriminating between Y and Y′ using fast Fourier transforms

FFT was performed locally on selected regions corresponding to different shear strain and rotation values in the top SrRuO$_3$ layers of the three samples, as shown in Fig. 5. The regions of interest are selected based on the largest contrast in the GPA rotation maps in Figs. 5(d)–5(f), and give the colored diffraction patterns in (a)–(c) for the sample with 90 u.c. (a), 45 u.c. (b), and 23 u.c. (c) PbTiO$_3$, respectively, combining the FFT Bragg peaks in red and in green from the two regions. For the samples with 90 and 45 u.c. PbTiO$_3$, the two diffraction patterns do not overlap perfectly, and a very small horizontal shift can be observed [the $(02\bar{2})_{pc}$ peak is enlarged for clarity]. For comparison, the diffraction pattern has been simulated for the Y and Y' orientations by arbitrarily increasing the difference between the a_o and b_o parameters (a_o = 5.62 and b_o = 5.48 in arbitrary units), making the difference in the Bragg peak positions more visible: the difference between Y and Y' results in horizontal shifts of peaks, as measured experimentally. No shift is observed for the SrRuO$_3$ top electrode above 23 u.c. PbTiO$_3$. From this, we can conclude that the contrast seen in the GPA strain and rotation maps for the two samples with the thickest PbTiO$_3$ layers arises from alternating Y and Y' domains. Moreover, Fig. 5(d) shows that the transition from Y to Y' domains for the sample with 90 u.c. PbTiO$_3$ is gradual with a modulation of the rotation following a sinusoidal behavior between 0.3° and −0.3° with a period of ∼30 nm. In comparison, this transition is much sharper for the sample with the 45 u.c. PbTiO$_3$ layer, with the modulation of the rotation following a step-like function between 0.15° and −0.2° with a period of ∼20 nm as shown in Fig. 5(e), hinting at the presence of proper twin boundaries between the Y and Y' domains. Further discussion and a high resolution

FIG. 5. FFT of Y/Y' oriented top SrRuO$_3$ regions of the samples with (a) 90 u.c. PbTiO$_3$ (b) 45 u.c. PbTiO$_3$ and (c) 23 u.c. PbTiO$_3$ compared to the simulation (g) with a_o = 5.62 and b_o = 5.48 parameters (in arbitrary units). The colored diffraction patterns of the top SrRuO$_3$ in (a)–(c) combine the FFT Bragg peaks of the Y domain in red and the Y' domain in green, where the regions of interest were selected based on the regions of largest contrast in the GPA rotation maps in (d)–(f).

TEM image of such a twin boundary is shown in the supplementary material, Sec. S4.

III. DISCUSSION

We show that the complex tilt pattern of the PbTiO$_3$ layer is responsible for the deformation of the SrRuO$_3$ layer deposited on top, resulting in the periodic pattern visible in the topography by AFM. Our STEM measurements highlight how the domain pattern in the PbTiO$_3$ layer affects the strain state and crystal orientation in the SrRuO$_3$ top layer, with clear differences for the three samples with different PbTiO$_3$ layer thicknesses.

We find that the top SrRuO$_3$ layers show a different behavior for each of the three samples, shown in Fig. 6, while the bottom SrRuO$_3$ layers systematically have the same orientation as the DyScO$_3$ substrate (X-orthorhombic orientation), probably pinned by the interfacial continuity of the oxygen octahedral rotation imposed by the substrate.

For the sample with a 23 u.c. PbTiO$_3$ layer, where no pattern is visible in the topography, we observe a flux-closure type PbTiO$_3$ domain structure and correspondingly a null or weakly distorted SrRuO$_3$ structure, homogeneously in the Y-orthorhombic orientation, as shown in Fig. 6 (bottom row).

For the sample with a 45 u.c. PbTiO$_3$ layer, where a pattern is only weakly observed in the topography, we again have a flux-closure type PbTiO$_3$ domain structure. However, in Fig. 3, if we compare the out-of-plane (e) and in-plane (h) strain maps close to the interfaces, the strain pattern locally resembles that of the a/c phase [Figs. 3(d) and 3(g)]. This points at a nascent a/c phase near the top interface, allowing a more pronounced deformation that translates into a clearly distorted SrRuO$_3$ structure that shares the same periodicity as the PbTiO$_3$. The top SrRuO$_3$ thus alternates between Y- and Y'-orthorhombic orientations—with a period corresponding to the period of the domain pattern in PbTiO$_3$. The mechanism that drives the rotation of the top SrRuO$_3$ is strain-induced: due to the small shear and rotation in the top layer of PbTiO$_3$, the PbTiO$_3$/top SrRuO$_3$ interface is not totally flat (left and right inclination). The formation of Y/Y' domains is a good way to minimize the interface strain [Fig. 6 (center row)].

Finally, in the sample with the 90 u.c. thick PbTiO$_3$ layer, where the topography displays noticeable tilts and trenches, the a/c-phase is fully developed, with strong PbTiO$_3$ lattice heterogeneity that partially imprints on the top SrRuO$_3$ electrode. Here, the top SrRuO$_3$ exhibits domains with alternating primary Y- and Y'-orthorhombic orientations, and some X interstitial regions. The positive and negative rotation on the SrRuO$_3$ correspond to the Y and Y' domains, as evidenced by the GPA shear strain and rotation maps. In between these Y and Y' domains, a very tiny X-orientated region is often observed in the FFT. This is typically restrained to a 10 nm width domain at the interface between the Y and Y' domains, where no rotation was observed on the GPA map. It is different from the case with the 45 u.c. thick PbTiO$_3$ layer, where sharp interfaces and no X oriented domain were observed between the Y and Y' domains.

Our work demonstrates that the large structural distortions associated with ferroelastic domains propagate through the top SrRuO$_3$ layer, creating a modulated structure that extends beyond the ferroelectric layer thickness, allowing domain engineering in the top SrRuO$_3$ electrode. Since there exists a one-to-one correspondence between the structural and magnetic domains,[12] our approach allows magnetic domain engineering in SrRuO$_3$ thin films through structural domain engineering to be realized. This work paves a new path toward control of magnetic domains via structural coupling to ferroelastic domains.
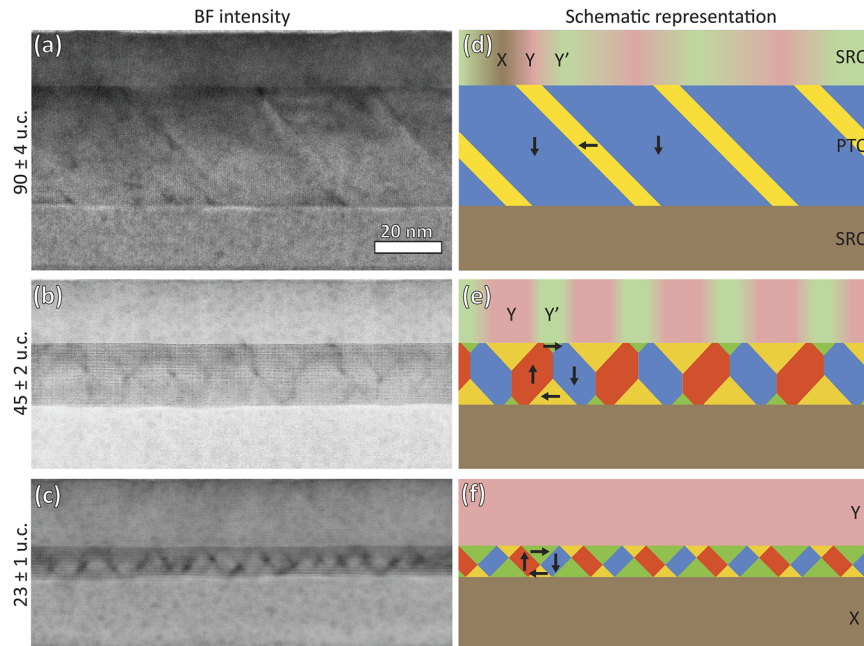
FIG. 6. STEM-BF images (a)–(c) on three different samples, together with the sketches (d)–(f) representing the different polarization patterns in the PbTiO$_3$ layers and the induced crystallographic domains in the top SrRuO$_3$ layers: (top row) 90±4 u.c., (center row) 45±2 u.c., and (bottom row) 23±1 u.c. thick PbTiO$_3$ between top and bottom SrRuO$_3$ electrodes (55±2 u.c. thick) on DyScO$_3$ substrates. From these images, the domain walls are visible in the PbTiO$_3$ layers, forming the expected a/c pattern for the thicker PbTiO$_3$ layer and transforming into a flux-closure pattern for the thinner PbTiO$_3$ layers. In the PbTiO$_3$ layers, domains with up polarization are shown in red, down in blue, left in yellow, and right in green. In the SrRuO$_3$ layers, the X (or X') orientation is shown in brown, Y in red, and Y' in green.

IV. EXPERIMENTAL TECHNIQUES

A. Sample growth

The three samples were deposited using our in-house constructed off-axis radio-frequency magnetron sputtering system, equipped with three different guns allowing the deposition of heterostructures and solid solutions of high crystalline quality. PbTiO$_3$ thin films were deposited at 560 °C, in 180 mTorr of a 20:29 O$_2$/Ar mixture, at a power of 60 W, and using a Pb$_{1.1}$TiO$_3$ target with 10% excess Pb to compensate for its volatility. SrRuO$_3$ layers were deposited from a stoichiometric target in 100 mTorr of an O$_2$/Ar mixture of ratio 3:60 at a power of 80 W. The bottom layer was grown at 640 °C, while for the top layer, the temperature was kept at the growth temperature used for PbTiO$_3$, i.e., 560 °C, to avoid possible damage of the PbTiO$_3$ layer. Huettinger PFG 300 RF power supplies are used in power control mode. The sample holder is grounded during deposition, but the sample surface is left floating.

B. Atomic force microscopy

Topography measurements were performed using a *Digital Instrument* Nanoscope Multimode DI4 with a *Nanonis* controller.

C. Scanning transmission electron microscopy

Cross-sectional slices prepared by a focus ion beam allow the imaging of domain structures by scanning transmission electron microscopy. Experiments were acquired on Nion Cs-corrected UltraSTEM200 at 100 kV operating voltage. A convergence angle of 30 mrad was used to allow high-resolution atomic imaging with a typical spatial resolution of 1 Å. Three imaging detectors in the STEM are used to simultaneously obtain bright field, annular bright field or medium angle annular dark field, and high angle annular dark field images. For ABF-MAADF imaging, the inner-outer angles can be continuously adjusted between 10–20 and 60–120 mrad. Most ABF images were collected with 15–30 mrad and MAADF images with 40–80 mrad angular ranges.

For the high-resolution HAADF images used to extract GPA, to minimize the influence of the sample drift and environmental noise, a series of fast-scan (low exposure time) HAADF images was taken in the same region; afterward, a script based on Gatan DigitalMicrograph software aligned and summed them together. This technique typically used 20 4k × 4k images with 1 μs exposure time per pixel.

GPA is an algorithm that reconstructs the displacement field $\vec{u}(\vec{r})$ from HAADF images by measuring the displacement of lattice fringes with respect to a reference lattice here chosen as the substrate. GPA thus allows the local strain present in the different layers to be revealed: in-plane strain $\varepsilon_{yy} = \frac{\partial u_y}{\partial y}$ (along [010]$_{pc}$, i.e., perpendicular to the growth direction), out-of-plane strain $\varepsilon_{zz} = \frac{\partial u_z}{\partial z}$ (along [001]$_{pc}$ i.e., along the growth direction), shear strain $\varepsilon_{yz} = \frac{1}{2}\left(\frac{\partial u_z}{\partial y} + \frac{\partial u_y}{\partial z}\right)$, and rotation $\omega_{yz} = \frac{1}{2}\left(\frac{\partial u_z}{\partial y} - \frac{\partial u_y}{\partial z}\right)$. This is particularly useful for the

study of the domain configuration in $PbTiO_3$, as the polarization is related to the strain from the strong strain-polarization coupling.[51] At room temperature, $PbTiO_3$ is tetragonal with the polarization pointing along the long tetragonal axis. The strain orientation and amplitude, therefore, indicate the orientation and magnitude of the polarization.

We determine the periodicity of the superstructures in the $PbTiO_3$ and $SrRuO_3$ layers by measuring the distances between the additional reciprocal space spots obtained after FFT. The accuracy of the measurement was estimated by considering the diffraction spot extension as the lower and upper limits for the superstructure length estimation.

D. X-ray diffraction

In-house XRD measurements were performed using a *Panalytical X'Pert* diffractometer with Cu $K\alpha_1$ radiation (1.540 598 0 Å) equipped with a 2-bounce Ge(220) monochromator and a triple axis detector. The θ-2θ scans were analyzed using the *InteractiveXRDFit* software.[52] This XRD system is also equipped with a PIXcel 1D detector, used for faster acquisition of reciprocal space maps.

SUPPLEMENTARY MATERIAL

supplementary material contains a detailed description of the orthorhombic orientations, with a schematic diagram showing the pseudocubic representation of the $(110)_o$-oriented $DyScO_3$ substrate and the six possible orthorhombic orientations of the $SrRuO_3$ on the substrate; reciprocal space maps showing the high crystalline quality of the samples studied here and demonstrating the periodic pattern of the $PbTiO_3$ layers; a table summarizing the different periods; and a discussion about the twin boundary observed in the $SrRuO_3$ layer above the 45 u.c. thick $PbTiO_3$ layer. Figure S2 showing the six possible orthorhombic orientations of $SrRuO_3$ on $(110)_o$-oriented $DyScO_3$ substrate can be found in high resolution here.

ACKNOWLEDGMENTS

IX AUTHOR DECLARATIONS
Conflict of Interest

The authors have no conflicts to disclose.

Author Contributions

C.L, M.H., A.G., and J.-M.T. designed the experiment. C.L., M.H., and L.T. grew the samples and conducted the AFM and XRD measurements and analysis. C.-P.S and A.G. conducted the STEM measurements. I.G., C.-P.S., and A.G. performed advanced STEM analysis. C.L. wrote the manuscript with contributions from all authors. All authors discussed the experimental results and models, commented on the manuscript, and agreed on its final version.

Céline Lichtensteiger: Conceptualization (equal); Data curation (equal); Formal analysis (equal); Funding acquisition (equal); Investigation (equal); Methodology (equal); Project administration (equal); Resources (equal); Software (equal); Supervision (equal); Validation (equal); Visualization (equal); Writing – original draft (equal); Writing – review & editing (equal). **Chia-Ping Su**: Data curation (equal); Formal analysis (equal); Investigation (equal); Methodology (equal); Resources (equal); Software (equal); Writing – original draft (equal); Writing – review & editing (equal). **Iaroslav Gaponenko**: Data curation (equal); Formal analysis (equal); Investigation (equal); Software (equal); Validation (equal); Visualization (equal); Writing – original draft (equal); Writing – review & editing (equal). **Marios Hadjimichael**: Data curation (equal); Investigation (equal); Methodology (equal); Validation (equal); Writing – original draft (equal); Writing – review & editing (equal). **Ludovica Tovaglieri**: Data curation (equal); Formal analysis (equal); Investigation (equal); Writing – original draft (equal); Writing – review & editing (equal). **Patrycja Paruch**: Conceptualization (equal); Funding acquisition (equal); Writing – original draft (equal); Writing – review & editing (equal). **Alexandre Gloter**: Conceptualization (equal); Funding acquisition (equal); Supervision (equal); Writing – original draft (equal); Writing – review & editing (equal). **Jean-Marc Triscone**: Conceptualization (equal); Funding acquisition (equal); Supervision (equal); Writing – review & editing (equal).

DATA AVAILABILITY

The data that support the findings of this study are available in Yareta at https://doi.org/10.26037/yareta: nt2pqmrilrc77nqy2yzjwdgtdu.

REFERENCES

[1]C. H. Ahn *et al.*, "Ferroelectric field effect in epitaxial thin film oxide $SrCuO_2/Pb(Zr_{0.52}Ti_{0.48})O_3$ heterostructures," Science **269**, 373–376 (1995).

[2]C. Eom *et al.*, "Single-crystal epitaxial thin films of the isotropic metallic oxides $Sr_{1-x}Ca_xRuO_3$ ($0 \leq x \leq 1$)," Science **258**, 1766–1769 (1992).

[3]G. Cao, S. McCall, M. Shepard, J. Crow, and R. Guertin, "Thermal, magnetic, and transport properties of single-crystal $Sr_{1-x}Ca_xRuO_3$ ($0 \leq x \leq 1.0$)," Phys. Rev. B **56**, 321–329 (1997).

[4]L. Wang *et al.*, "Ferroelectrically tunable magnetic skyrmions in ultrathin oxide heterostructures," Nat. Mater. **17**, 1087–1094 (2018).

[5]S. D. Seddon *et al.*, "Real-space observation of ferroelectrically induced magnetic spin crystal in $SrRuO_3$," Nat. Commun. **12**, 2007 (2021).

[6]R. Dirsyte *et al.*, "Impact of epitaxial strain on the ferromagnetic transition temperature of $SrRuO_3$ thin films," Thin Solid Films **519**, 6264–6268 (2011).

[7]G. Koster *et al.*, "Structure, physical properties, and applications of $SrRuO_3$ thin films," Rev. Mod. Phys. **84**, 253–298 (2012).

16 October 2023 08:57:33

[8] J. C. Jiang, W. Tian, X. Pan, Q. Gan, and C. B. Eom, "Effects of miscut of the SrTiO₃ substrate on microstructures of the epitaxial SrRuO₃ thin films," Mater. Sci. Eng. B **56**, 152–157 (1998).

[9] J. C. Jiang, W. Tian, X. Q. Pan, Q. Gan, and C. B. Eom, "Domain structure of epitaxial SrRuO₃ thin films on miscut (001) SrTiO₃ substrates," Appl. Phys. Lett. **72**, 2963–2965 (1998).

[10] A. Vailionis, W. Siemons, and G. Koster, "Room temperature epitaxial stabilization of a tetragonal phase in ARuO₃ (A = Ca and Sr) thin films," Appl. Phys. Lett. **93**, 051909 (2008).

[11] N. D. Zakharov, K. M. Satyalakshmi, G. Koren, and D. Hesse, "Substrate temperature dependence of structure and resistivity of SrRuO₃ thin films grown by pulsed laser deposition on (100) SrTiO₃," J. Mater. Res. **14**, 4385–4394 (1999).

[12] W. Wang et al., "Magnetic domain engineering in SrRuO₃ thin films," Npj Quantum Mater. **5**, 73 (2020).

[13] Y. Tang et al., "Periodic polarization waves in a strained, highly polar ultrathin SrTiO₃," Nano Lett. **21**, 6274–6281 (2021).

[14] M. Hadjimichael et al., "Metal–ferroelectric supercrystals with periodically curved metallic layers," Nat. Mater. **20**, 495–502 (2021).

[15] N. A. Pertsev, A. G. Zembilgotov, and A. K. Tagantsev, "Effect of mechanical boundary conditions on phase diagrams of epitaxial ferroelectric thin films," Phys. Rev. Lett. **80**, 1988–1991 (1998).

[16] N. A. Pertsev and V. G. Koukhar, "Polarization instability in polydomain ferroelectric epitaxial thin films and the formation of heterophase structures," Phys. Rev. Lett. **84**, 3722 (2000).

[17] V. G. Koukhar, N. A. Pertsev, and R. Waser, "Thermodynamic theory of epitaxial ferroelectric thin films with dense domain structures," Phys. Rev. B **64**, 214103 (2001); arXiv:cond-mat/0102460.

[18] Y. L. Li, S. Y. Hu, Z. K. Liu, and L. Q. Chen, "Phase-field model of domain structures in ferroelectric thin films," Appl. Phys. Lett. **78**, 3878–3880 (2001).

[19] Z. Jiang et al., "Strain-induced control of domain wall morphology in ultrathin PbTiO₃ films," Phys. Rev. B **89**, 35–37 (2014).

[20] J. B. Chapman, A. V. Kimmel, and D. M. Duffy, "Novel high-temperature ferroelectric domain morphology in PbTiO₃ ultrathin films," Phys. Chem. Chem. Phys. **19**, 4243–4250 (2017).

[21] D. G. Schlom et al., "Strain tuning of ferroelectric thin films," Annu. Rev. Mater. Res. **37**, 589–626 (2007).

[22] C. Kittel, "Theory of the structure of ferromagnetic domains in films and small particles," Phys. Rev. **70**, 965–971 (1946).

[23] C. Lichtensteiger, S. Fernandez-Pena, C. Weymann, P. Zubko, and J. M. Triscone, "Tuning of the depolarization field and nanodomain structure in ferroelectric thin films," Nano Lett. **14**, 4205–4211 (2014); arXiv:1507.08498.

[24] C. Lichtensteiger, C. Weymann, S. Fernandez-Pena, P. Paruch, and J. M. Triscone, "Built-in voltage in thin ferroelectric PbTiO₃ films: The effect of electrostatic boundary conditions," New J. Phys. **18**, 043030 (2016).

[25] A. K. Yadav et al., "Observation of polar vortices in oxide superlattices," Nature **530**, 198–201 (2016).

[26] V. A. Stoica et al., "Optical creation of a supercrystal with three-dimensional nanoscale periodicity," Nat. Mater. **18**, 377–383 (2019).

[27] M. Hadjimichael, "Ferroelectric domains in lead titanate heterostructures," Ph.D. thesis, University College London, 2019.

[28] M. A. Gonçalves, C. Escorihuela-Sayalero, P. Garca-Fernández, J. Junquera, and J. Íñiguez, "Theoretical guidelines to create and tune electric skyrmion bubbles," Sci. Adv. **5**, eaau7023 (2019).

[29] S. Das et al., "Observation of room-temperature polar skyrmions," Nature **568**, 368–372 (2019).

[30] Y. J. Wang et al., "Polar meron lattice in strained oxide ferroelectrics," Nat. Mater. **19**, 881 (2020).

[31] J. Íñiguez, P. Zubko, I. Luk'yanchuk, and A. Cano, "Ferroelectric negative capacitance," Nat. Rev. Mater. **4**, 243 (2019).

[32] A. H. Vlooswijk et al., "Smallest 90° domains in epitaxial ferroelectric films," Appl. Phys. Lett. **91**, 20–23 (2007); arXiv:0706.2487.

[33] G. Catalan et al., "Flexoelectric rotation of polarization in ferroelectric thin films," Nat. Mater. **10**, 963–967 (2011).

[34] O. Nesterov et al., "Thickness scaling of ferroelastic domains in PbTiO₃ films on DyScO₃," Appl. Phys. Lett. **103**, 142901 (2013).

[35] C. Lichtensteiger et al., "Mapping the complex evolution of ferroelastic/ferroelectric domain patterns in epitaxially strained PbTiO₃ heterostructures," APL Mater. **11**, 061126 (2023).

[36] B. Veličkov, V. Kahlenberg, R. Bertram, and M. Bernhagen, "Crystal chemistry of GdScO₃, DyScO₃, SmScO₃ and NdScO₃," Z. Kristallogr. **222**, 466–473 (2007).

[37] J. J. Randall and R. Ward, "The preparation of some ternary oxides of the platinum metals¹,²," J. Am. Chem. Soc. **81**, 2629–2631 (1959).

[38] A. M. Glazer, "The classification of tilted octahedra in perovskites," Acta Crystallogr., Sect. B: Struct. Crystallogr. Cryst. Chem. **28**, 3384–3392 (1972).

[39] P. M. Woodward, "Octahedral tilting in perovskites. I. Geometrical considerations," Acta Crystallogr., Sect. B: Struct. Sci. **53**, 32–43 (1997).

[40] Although the strain with respect to a_0 is compressive, the system is usually referred to as being under tensile strain because the lattice parameter of DyScO₃ is larger than the bulk $a = b$ axes of PbTiO₃.

[41] M. J. Highland et al., "Interfacial charge and strain effects on the ferroelectric behavior of epitaxial (001) PbTiO₃ films on (110) DyScO₃ substrates," Appl. Phys. Lett. **104**, 132901 (2014).

[42] J. Junquera and P. Ghosez, "Critical thickness for ferroelectricity in perovskite ultrathin films," Nature **422**, 506–509 (2003).

[43] P. Aguado-Puente and J. Junquera, "Ferromagneticlike closure domains in ferroelectric ultrathin films: First-principles simulations," Phys. Rev. Lett. **100**, 177601 (2008).

[44] M. Stengel, D. Vanderbilt, and N. A. Spaldin, "Enhancement of ferroelectricity at metal-oxide interfaces," Nat. Mater. **8**, 392–397 (2009).

[45] S. Li et al., "Periodic arrays of flux-closure domains in ferroelectric thin films with oxide electrodes," Appl. Phys. Lett. **111**, 052901 (2017).

[46] M. Hadjimichael, Y. Li, L. Yedra, B. Dkhil, and P. Zubko, "Domain structure and dielectric properties of metal-ferroelectric superlattices with asymmetric interfaces," Phys. Rev. Mater. **4**, 094415 (2020).

[47] Y. L. Tang et al., "Observation of a periodic array of flux-closure quadrants in strained ferroelectric PbTiO₃ films," Science **348**, 547–551 (2015).

[48] S. Li et al., "Evolution of flux-closure domain arrays in oxide multilayers with misfit strain," Acta Mater. **171**, 176–183 (2019).

[49] M. J. Hÿtch, E. Snoeck, and R. Kilaas, "Quantitative measurement of displacement and strain fields from HREM micrographs," Ultramicroscopy **74**, 131–146 (1998).

[50] Although the orientation of the lamella does not allow us to discriminate between X and X', we can go one step further by discriminating between Y and Y', the two orientations corresponding to very small horizontal shift in the peak positions.

[51] R. E. Cohen and H. Krakauer, "Electronic structure studies of the differences in ferroelectric behavior of BaTiO₃ and PbTiO₃," Ferroelectrics **136**, 65 (1992).

[52] C. Lichtensteiger, "InteractiveXRDFit: A new tool to simulate and fit X-ray diffractograms of oxide thin films and heterostructures," J. Appl. Crystallogr. **51**, 1745–1751 (2018).